Rapid formation of hydroxymethyl hydroperoxide and its vital role in methanesulfonic acid-methylamine nucleation: impacts of urban industrial areas

Rongrong Li ‡, Zeyao Li ‡, Chengyan Zhang, Rui Wang*, Jihuan Yang, Heran Cui, Xuanye Li, Nini Huo, Tianlei Zhang*

Institute of Theoretical and Computational Chemistry, Shaanxi Key Laboratory of Catalysis, School of Chemical & Environment Science, Shaanxi University of Technology, Hanzhong, Shaanxi, 723000, P. R. China

Abstract

Organic peroxides are widely recognized as important contributors to secondary organic aerosols formation. Among these, hydroxymethyl hydroperoxide (HMHP) is a common species found in both the gas phase and fine aerosols. Despite its abundance, the molecular-level formation of HMHP through methanesulfonic acid (MSA)-catalyzed hydrolysis of CH_2OO, particularly in the gas phase and at the air-water interface, remains insufficiently examined. Moreover, the role of HMHP in new particle formation (NPF) has not been fully elucidated. Herein, we employ quantum chemical calculations together with Born-Oppenheimer molecular dynamics simulations to investigate HMHP formation from CH_2OO hydrolysis with MSA under both gas phase and interfacial conditions. Our results show that HMHP forms rapidly and stably in both environments. Further analysis using the atmospheric cluster dynamics code reveals that HMHP not only enhances the clustering stability of MSA-methylamine (MA) clusters, but also exerts a direct role in promoting MSA-MA nucleation. Importantly, in regions with elevated HMHP concentrations (3.00×10^{10} - 1.25×10^{11} molecules·cm^{-3}), such as Niwot Ridge and Southeastern United States, the HMHP-involved pathways contribute unexpectedly up to 42% and 59% of total nucleation flux at 258.15 K, respectively. These findings provide new insights into HMHP formation pathways and the efficient MSA-MA-HMHP nucleation mechanism, offering a plausible explanation for the frequent and intense NPF events observed in continental regions.

Keywords: hydroxymethyl hydroperoxide; gas phase; interfacial; new particle formation

* Corresponding authors. Tel: +86-0916-2641083, Fax: +86-0916-2641083.

e-mail: wangrui830413@163.com (R. Wang) ztianlei88@l63.com (T. L Zhang)

‡ These authors contributed equally to this work.

1. Introduction

Organic peroxides serve as important reactive intermediates in atmospheric oxidation processes, facilitating free radical chain termination, oxidant cycling, and the formation of aerosols (Wang et al., 2023; Tröstl et al., 2016). Among these, hydroxymethyl hydroperoxide (HMHP), a product of the hydrolysis of the simplest and highest concentrations criegee Intermediates (CH_2OO), has been detected at notable concentrations in the atmosphere (Lee et al., 1993; Nguyen et al., 2015). Atmospheric concentrations of HMHP typically range around 10^9 molecules·cm^{-3} in locations such as Central Portugal (Jackson and Hewitt, 1996), Pabstthum (Grossmann et al., 2003) and Beijing (Yi, 2000). However, in regions like Guangzhou (Zhang et al., 2001) and Niwot Ridge (Hewitt and Kok, 1991), these levels can increase to approximately 10^{10} molecules·cm^{-3}. Notably, in the Southeastern United States (Allen et al., 2018), concentrations can even reach up to 10^{11} molecules·cm^{-3}. Due to its high abundance, HMHP undergoes subsequent reactions with other atmospheric species, leading to the formation of hydroperoxides, organic peroxides, and secondary organic aerosols, which play a crucial role in influencing air quality, climate forcing, and human health (Sakamoto et al., 2013; Rissanen et al., 2014). So, understanding the source of HMHP and its impact on the atmospheric environment has become a major topic of significant interest in atmospheric chemistry.

HMHP is formed predominantly through the hydrolysis of CH_2OO, a process that has been extensively investigated through both experimental studies (Chao et al., 2015; Stone et al., 2014; Berndt et al., 2015) and theoretical simulations (Wu et al., 2023a; Lin et al., 2016; Wu et al., 2023b). Experimental data (Chao et al., 2015; Ouyang et al., 2013) estimate the rate constant for the direct CH_2OO hydrolysis to from HMHP to be approximately 4×10^{-15} cm^3 molecule^{-1} s^{-1}. In contrast, hydrolysis involving the water dimer ($(H_2O)_2$) has rate constants between 4×10^{-12} and 8.9×10^{-12} cm^3 molecule^{-1} s^{-1} at 294-298 K (Lin et al., 2016; Berndt et al., 2015), approximately three orders of magnitude higher than that of the reaction with monomeric water, demonstrating that the presence of the water dimer significantly enhances the hydrolysis rate (Long et al., 2016; Anglada and Solé, 2016; Newland et al., 2015). Additionally, quantum chemical calculations have shown that atmospheric organic amines, acids, and alcohols can catalyze CH_2OO hydrolysis by substantially lowering activation barriers and accelerating reaction rates (Zhang et al., 2018; Chao et al., 2019). However, the role of methanesulfonic acid (MSA) in faciliating CH_2OO hydrolysis remains underexplored, even through the calculations reported by several groups (Li et al., 2024c; Wang et al., 2025) have shown that MSA is a notably effective catalyst in both CH_3CHOO and $HNSO_2$ hydrolysis. In fact, MSA is a major oxidation product of organosulfur compounds originating from a variety of sources, including biological processes, biomass combustion, industrial emissions, and agricultural activities. As a result, it has been

widely detected in atmospheric aerosol particles across diverse geographic regions, spanning from coastal to inland areas (Barnes et al., 2006; Gaston et al., 2010). Notably, in coastal regions characterized by elevated MSA levels, MSA concentrations range from approximately 10% to 250% of gaseous sulfuric acid concentration (Ning et al., 2022; Ning and Zhang, 2022), whereas in continental regions with lower MSA levels, including many inland urban and industrial regions, MSA concentrations are typically on the order of ~10%-50% of gaseous sulfuric acid concentrations (Berresheim et al., 2002; Chen et al., 2020). Furthermore, MSA is characterized by strong acidity and the ability to act as a proton-transfer bridge, suggesting a potentially important role in modulating the hydrolysis of CH_2OO. So, the lack of understanding of the MSA-catalyzed CH_2OO hydrolysis reaction mechanism limits the accurate understanding and evaluation of HMHP formation, especially in regions with high MSA pollution concentrations.

Interfacial reactions at the air-water interface complement gas-phase reactions and can significantly influence reaction rates (Xu et al., 2024; Fang et al., 2024). These interfacial reactions may involve distinct mechanisms, with interfacial water molecules not only serving as reactive sites but also participating directly as reactants, proton transfer mediators, and both donors and acceptors (Tang et al., 2024). For example, MSA-assisted $HNSO_2$ hydrolysis at the air-water interface follows two distinct reaction mechanisms, the ion-forming mechanism and the proton exchange mechanism, resulting in the formation of the $SFA^{-}\cdots H_3O^{+}$ ion pair. This contrasts with the gas-phase production of SFA formed from the MSA-catalyzed hydrolysis of $HNSO_2$ (Wang et al., 2025). In addition, the reaction between glyoxal and dimethylamine proceeds 5.70×10^4 times more rapidly at aqueous interfaces compared to the gas phase, where it is less likely to take place (Dong et al., 2024). Therefore, based on gas-phase reactions, it is essential to investigate the MSA-catalyzed CH_2OO hydrolysis reaction mechanisms at the air-water interface, which will enrich the understanding of HMHP sources in regions affected by MSA pollution.

MSA, structurally and chemically similar to the atmospheric aerosol nucleating precursor H_2SO_4, is regarded as an important nucleating precursor for NPF (Elm, 2021; Hodshire et al., 2019). With stringent global regulations reducing SO_2 emissions from fossil fuels (Perraud et al., 2015; Li et al., 2024b), MSA's role in NPF has received widespread attention. Previous studies have investigated the effects of organic compounds (HCOOH, CH_3COOH, CH_3OH, CH_2O, CH_3COCH_3, $C_2H_5OC_2H_5$, $HCOOCH_3$, $H_2C_2O_4$) (Zhao et al., 2017; Xu et al., 2017a; Arquero et al., 2017; Xu et al., 2017b), iodic acid-containing (HIO_2, HIO_3) (Ning et al., 2022; Wu et al., 2023c) and bases (NH_3, CH_3NH_2 (MA), $(CH_3)_2NH$, $(CH_3)_3N$) (Chen et al., 2016; Wen et al., 2018; Shen et al., 2020; Liu et al., 2022) on MSA-driven binary nucleation, identifying MA as the most effective base in promoting MSA-driven NPF. However,

the binary MSA-MA nucleation mechanism is insufficient to explain the high NPF rates observed under realistic atmospheric conditions. This implies that other potential gaseous precursors may participate in and further enhance binary MSA-MA nucleation (Lee et al., 2019; Zhang et al., 2022). As a result, organic acids (Zhang et al., 2022) and inorganic acids (Hu et al., 2023) have been proved to enhance the formation rate of MSA-MA-driven ternary nucleation in areas with abundant specific pollutants. However, as one of the organic peroxides, the HMHP involved in MSA-MA-driven NPF remains unexplored. This will limit our knowledge of frequent NPF events, especially in urban industrial areas.

In this work, the gaseous and interfacial formation mechanisms of HMHP catalyzed by MSA, as well as its crucial role in MSA-MA nucleation, were explored. Specifically, quantum chemical calculations and Born-Oppenheimer molecular dynamics (BOMD) simulations were employed to elucidate the reaction mechanism of MSA-mediated CH_2OO hydrolysis leading to the formation of HMHP in both the gas phase and at the air-water interface. Subsequently, the potential effect of HMHP in the MSA-MA-dominated NPF process was assessed under a series of atmospheric conditions, utilizing quantum chemical calculation combined with the Atmospheric Cluster Dynamics Code (ACDC). This work will not only enhances the understanding of HMHP formation but also contributes to explaining some unexplained fluxes in NPF, while highlighting the significant impact of HMHP on nucleation processes.

2. Methods

2.1 Quantum Chemical Calculations

To investigate the MSA-assisted CH_2OO hydrolysis in the gas phase, geometric configurations and vibrational frequencies of all relevant configurations, including reactants, pre-reactive complexes, transition states (TSs), post-reactive complexes, and products, were calculated at the M06-2X/6-311++G(2df,2pd) level (Mardirossian and Head-Gordon, 2016; Pereira et al., 2017) using Gaussian 09. Intrinsic reaction coordinate analyses, performed at the same computational level, verified the correspondence of each TS to its associated pre- and post-reactive complexes. Subsequently, the ORCA 4.2.0 package (Neese, 2012) was performed to compute the single point energies using the CCSD(T)-F12/cc-pVDZ-F12 method.

To identity the global minimum energy configurations of $(MSA)_x(MA)_y(HMHP)_z$ clusters, the ABCluster program (Zhang and Dolg, 2015) was utilized to systematically generate initial configurations for various clusters. Subsequently, these structures were further optimized using different levels of theoretical methods. Specifically, the ABCluster program generated $n \times 1000$ ($1 < n \leq 4$) initial structures for each cluster system. Then, the PM6 semi-

empirical method (Partanen et al., 2016) was used for preliminary optimization of these structures. As the M06-2X functional performs well for noncovalent binding and structural predictions of thermochemical and atmospheric aggregates, 100 of the lowest-energy configurations were chosen from $n \times 1000$ ($1 < n \leq 3$) structures and re-optimized using M06-2X/6-31G(d,p). Next, the 10 most stable configurations were re-optimized at the M06-2X/6-311++G(2df,2pd) level, and the configuration with the lowest free energy was identified. Ultimately, single-point energies were evaluated at the DLPNO-CCSD(T)-F12/cc-pVDZ-F12-CABS level (Tsona Tchinda et al., 2022) in ORCA, using geometries optimized for the stable clusters at the M06-2X/6-311++G(2df,2pd) level.

2.2 Rate coefficient calculations

The rate coefficients of MSA-mediated CH_2OO hydrolysis were investigated through a two-step approach. Initially, high-pressure-limit (HPL) rate coefficients were obtained using the VRC-VTST (Zhang et al., 2023; Zhang et al., 2024) approach implemented in Polyrate 2017-C (Meana-Pañeda et al., 2024). Subsequently, MESMER (Master Equation Solver for Multi-Energy Well Reactions) (Glowacki et al., 2012) was employed to calculate the rate coefficients of MSA-catalyzed CH_2OO hydrolysis across the temperature range of 280.0-320.0 K. The rate coefficients for the barrierless transition from separated reactants to pre-reactive complexes were estimated using the Inverse Laplace Transform (ILT) (Kumar et al., 2021) method. Concurrently, RRKM theory was employed to calculate the rate coefficients describing the conversion of the pre-reactive complex into the post-reactive species through the transition state. Further descriptions of the ILT methods and RRKM theory are provided in Parts S1 and S2 of the Supplement, respectively.

2.3 Born-Oppenheimer Molecular Dynamic (BOMD) simulation

BOMD calculations were carried out in CP2K program (Hutter et al., 2014), with exchange and correlation interactions described by the BLYP functional (Becke, 1988). Dispersion effects were incorporated through Grimme's dispersion (Grimme et al., 2010) (BLYP-D3) method. The Goedecker-Teter-Hutter (GTH) (Goedecker et al., 1996) pseudopotential was adopted for the core region, whereas the valence electrons were represented through a Gaussian DZVP basis (Phillips et al., 2005) in conjunction with an auxiliary plane-wave set. The calculations employed a plane-wave energy cutoff of 280 Ry together with a 40 Ry cutoff for the Gaussian basis set. In the gas phase, a supercell with a side length of 15 Å was employed to minimize periodic boundary effects, and the integration was performed with a 0.5 fs time step. A water droplet containing 191 molecules, serving as the interfacial model, was subjected to BOMD pre-optimization for roughly 5.0 ps at 300 K. CH_2OO and MSA were then positioned at the air-water interface, followed by 10 ps of molecular dynamics simulation. A supercell length

of 35 Å was adopted to prevent interactions between periodic images of the droplet, while the dynamics were advanced with a timestep of 1.0 fs. The gas-phase and interfacial simulations were conducted under NVT conditions at ~300 K, with the temperature maintained via a Nosé-Hoover thermostat.

2.4 Atmospheric Clusters Dynamic Code (ACDC) Model

ACDC (McGrath et al., 2012) was utilized to investigate the cluster formation rates, steady-state cluster concentrations, and growth mechanisms within the extensive MSA-MA-HMHP system. Thermodynamic data, calculated at the DLPNO-CCSD(T)-F12/cc-pVDZ-F12-CABS//M06-2X/6-311++G(2df,2pd) level of theory, were employed as input parameters for the ACDC simulations. The temporal progression of cluster concentrations was numerically resolved by solving the birth-death equations, employing the ode15s solver within the MATLAB-R2013a program. The birth-death equations are given below,

$$\frac{dc_i}{dt} = \frac{1}{2}\sum_{j<i}\beta_{j,(i-j)}C_jC_{(i-j)} + \sum_j \gamma_{(i+j)\to i}C_{i+j} - \sum_j \beta_{i,j}C_iC_j - \frac{1}{2}\sum_{j<i}\gamma_{i\to j}C_i + Q_i - S_i \quad (1)$$

In this formulation, c_i denotes the concentration of cluster i, $\beta_{i,j}$ represents the collision coefficient of clusters i with j and then $\gamma_{(i+j)\to i}$ represents the evaporation coefficient of clusters evaporating from $i + j$ to i and j clusters. Q_i represents the potential source for cluster i, while S_i denotes the sink term for cluster i. External losses of cluster i were represented using a fixed condensation sink coefficient of 0.02 s^{-1} (Qiao et al., 2024; Zhang et al., 2022). Besides, the clusters $(MSA)_4\cdot(MA)_3$ and $(MSA)_4\cdot(MA)_4$ were selected as boundary clusters in the MSA-MA-HMHP system, as boundary clusters in ACDC are required to be sufficiently stable to allow continued growth.

3. Results and discussion

3.1 The hydrolysis of CH_2OO with MSA in the gas phase

To evaluate the catalytic role of MSA in the CH_2OO hydrolysis reaction, the potential energy surface was investigated both in the presence and absence of MSA and H_2O. As depicted in Fig. 1(a) and (b), the potential energy surfaces with and without water closely match previously reported data (Wang et al., 2021a; Wang et al., 2021b), suggesting that the CCSD(T)-F12/cc-pVDZ-F12//M06-2X/6-311++G(2df,2pd) method is suitable for assessing MSA's catalytic effect. The MSA-catalyzed CH_2OO hydrolysis reaction (Fig. 1(c)) follows a continuous bimolecular process, involving $CH_2OO\cdots H_2O$ + MSA and $MSA\cdots H_2O$ + CH_2OO. The stabilization energy of $MSA\cdots H_2O$ is 9.8 kcal·mol^{-1} higher than that of $CH_2OO\cdots H_2O$. Considering the atmosphere concentrations of MSA (Li et al., 2024b), H_2O (Anglada et al., 2013), and CH_2OO (Khan et al., 2018), the concentration of $MSA\cdots H_2O$ is two orders of magnitude greater than that of $CH_2OO\cdots H_2O$, as shown in Table S3, predicting that the $MSA\cdots H_2O$ +

CH_2OO route is the dominant pathway for the MSA-catalyzed reaction. Starting from MSA···H_2O + CH_2OO, the reaction proceeds through the IM_MSA intermediate, which has stabilization energy 6.5 kcal·mol^{-1} and 0.7 kcal·mol^{-1} higher than IM and IM_WM, respectively. The increase in stabilization energy is primarily due to the addition of MSA, which reduces ring strain and favours C-O bond formation. Atoms in Molecules (AIM) topological analysis results also show that in IM_MSA ($\rho = 3.74 \times 10^{-2}$), the strength of the density of all electrons (C-O) is 1.64 times stronger than in IM_WM ($\rho = 2.27 \times 10^{-2}$), further stabilizing the intermediate. The reaction then proceeds through the barrierless transition state TS_MSA, forming a nine-membered ring complex $HOCH_2OOH$···MSA (labeled as IMF_MSA). This process has a 1.4 kcal·mol^{-1} lower energy barrier compared to the H_2O-catalyzed reaction, due to MSA's enhanced ability to facilitate proton transfer. Additionally, IMF_MSA is more stable by 7.6 kcal·mol^{-1} compared to IMF_WM.

To further examine the impact of MSA on the CH_2OO hydrolysis reaction, we calculated the effective rate constants for the CH_2OO hydrolysis assisted by H_2O ([H_2O] = 10^{15}-10^{17} molecules·cm^{-3}), NH_3 ([NH_3] = 10^{7}-10^{11} molecules·cm^{-3}), H_2SO_4 ([H_2SO_4] = 10^{4}-10^{8} molecules·cm^{-3}) and MSA ([MSA] = 10^{4}-10^{8} molecules·cm^{-3}) in Table S5. When the MSA concentration ranges from 10^{6} to 10^{8} molecules·cm^{-3}, its catalytic effect is substantially stronger than that of NH_3 ([NH_3] = 10^{7}-10^{11} molecules·cm^{-3}), with k'_{MSA} being approximately 2-6 orders of magnitude over the temperature range of 280.0-320.0 K. Similarly, for MSA concentrations between 10^{5} and 10^{8} molecules·cm^{-3}, MSA exhibits a significantly higher catalytic activity than SA ([SA] = 10^{4}-10^{7} molecules·cm^{-3}). In this case, k'_{MSA} exceeds k'_{SA} by about 1-3 orders of magnitude. Taken together, these results demonstrate that MSA is a more effective catalyst than both NH_3 and SA under atmospherically relevant conditions. Nevertheless, even under extreme conditions, with MSA at its upper-limit concentration ([MSA] = 10^{8} molecules·cm^{-3}) and H_2O at its lower-limit concentration ([H_2O] = 10^{16} molecules·cm^{-3}), k'_{MSA} is approximately five orders of magnitude smaller than $k'_{WM,}$ indicating that the catalytic efficiency of MSA remains lower than that of H_2O.

3.2 The hydrolysis of CH_2OO with MSA at the air-water interface

The mechanism of MSA-catalyzed CH_2OO hydrolysis at the air-water interface remained unclear. To elucidate this process, BOMD simulations were employed to investigate possible reaction pathways at the aqueous interface. Based on analogies with CH_2OO reactions involving other atmospheric species (Ding et al., 2024; Li et al., 2023; Cheng et al., 2025), three potential routes were considered: (*i*) MSA interacting with adsorbed CH_2OO at the air-water interface, (*ii*) CH_2OO interacting with adsorbed MSA at the air-water interface, or (*iii*) the MSA-CH_2OO complex reacting at the air-water interface. Because both CH_2OO and MSA exhibit high reactivity toward interfacial

water, their lifetimes at the droplet interface remain very brief, making pathway (*i*) and (*ii*) far less likely than pathway (*iii*). Therefore, only the reaction of the MSA···CH_2OO complex at the aqueous interface was considered, owing to its high stability in the gas phase.

As displayed in Fig. 2, Fig. S1, and Movie S1, the MSA···CH_2OO complex initially interacts with a water molecule at the aqueous interface. At 0.76 ps, this water molecule forms both a van der Waals interaction with the carbon atom in CH_2OO (d(C-O3) = 4.00 Å) and a hydrogen bond with the oxygen atom in MSA (d(O4-H2) = 3.27 Å), thereby generating a nine-membered ring structure (CH_2OO···MSA···H_2O). As the reaction progresses, a hydration transition-state-like ring configuration forms at 1.06 ps, with the C-O3, O4-H2 and O2-H1 bonds shorten to 1.75 Å, 1.27 Å and 0.97 Å, respectively, while the O3-H2 and O1-H1 bonds elongate to 1.16 Å and 1.85 Å, respectively. By 1.16 ps, the bond lengths of C-O3, O4-H2 and O2-H1 further shorten to 1.43 Å, 1.05 Å and 0.96 Å, while the O3-H2 and O1-H1 bonds further increase to 1.61 Å and 1.93 Å, respectively, indicating the formation of the hydrogen-bonded CH_2OOHOH···MSA complex. During this process, the interfacial water molecule acts as a reactant, with MSA serving as a proton transfer bridge. Notably, due to the higher abundance of interfacial water molecules compared to MSA, the formation of HMHP at the interface primarily proceeds through the direct hydration of CH_2OO. However, the source of HMHP from MSA-catalyzed CH_2OO hydrolysis at the interface occurs at a significantly faster rate than its corresponding gas-phase formation, with a computed ratio (r_1) of 1.01×10^2 at 298.0 K, which is detailed computational results are provided in Part S3. Traditionally, the loss of CH_2OO in the troposphere has been primarily attributed to its hydrolysis. Therefore, it is crucial to examine the rate ratio r_2 (equation (S4)) between interfacial MSA-catalyzed CH_2OO hydrolysis and the corresponding gas-phase process mediated by water. At 298.0 K, r_2 is 13.4, indicating that the formation of HMHP from interfacial MSA-mediated CH_2OO hydrolysis is much closer to that catalyzed by water in the gas phase. These results indicate that interfacial MSA-catalyzed CH_2OO hydrolysis is a significant source of HMHP formation in MSA-polluted areas under relatively humid conditions. Consequently, when evaluating the comprehensive sources of HMHP in MSA-rich regions, it is essential to consider the formation involving MSA-catalyzed hydrolysis of CH_2OO at the air-water interface.

3.3 The significance of HMHP in MSA-MA nucleation

The role of HMHP on MSA-MA-driven ternary nucleation was assessed. Initial assessments focused on the potential interaction sites of HMHP with MSA and MA, followed by an analysis of the conformation and stability of the $(MSA)_x(MA)_y(HMHP)_z$ ($0 \leqslant y \leqslant x + z \leqslant 3$) clusters. The MSA-MA nucleation mechanism involving

HMHP was then examined, along with the effects of temperature and precursor concentrations on the MSA-MA-HMHP system. Finally, the atmospheric implication of HMHP for MSA-MA nucleation were calculated for urban industrial areas.

3.3.1 Cluster conformational analysis

The formation of stable clusters is primarily dictated by the pronounced coupling of nucleation precursors (Ning et al., 2024; Li et al., 2024a; Li et al., 2024b). The electrostatic potential (ESP)-mapped molecular van der Waals (vdW) surface was computed to characterize the binding potential of HMHP with MSA and MA and to locate the corresponding interaction sites (Fig. 3(a)). The analysis revealed that HMHP exhibits a positive ESP value (+54.09 kcal·mol^{-1}) at the H atom of its -OH group, indicating its role as a hydrogen bond (HB) donor, while the oxygen atom of the -COOH shows a negative ESP of -32.68 kcal·mol^{-1}, indicating its role as a hydrogen bond acceptor. Thus, HMHP possesses dual functionalities as a HB donor and acceptor, allowing its association with the nucleating precursors MSA and MA, thereby generating HBs that stabilize the MSA-MA-HMHP clusters. Based on the ESP analysis, the most stable configurations of $(MSA)_x(MA)_y(HMHP)_z$ clusters were obtained (Fig. S2), and the actual binding sites within the ternary clusters were found to be consistent with the predictions from the ESP analysis.

To further access the non-covalent interactions within the $(MSA)_x(MA)_y(HMHP)_z$ clusters, the reduced density gradient (RDG) analysis was performed on representative clusters, including $(MSA)_1\cdot(MA)_1$, $(MSA)_1\cdot(MA)_1\cdot(HMHP)_1$ and $(MSA)_1\cdot(MA)_1\cdot(HMHP)_2$ cluster (Fig. 3(b)). In the RDG analysis, the blue region corresponds to strong attractions, similar to HBs, within the system. When compared to the $(MSA)_1\cdot(MA)_1$ cluster, the $(MSA)_1\cdot(MA)_1\cdot(HMHP)_1$ cluster exhibits two additional blue spikes, suggesting that HMHP forms strong interactions, particularly HBs, with MSA and MA. Moreover, the dominant blue spike in the $(MSA)_1\cdot(MA)_1\cdot(HMHP)_2$ cluster is shifted further leftward compared to that in the $(MSA)_1\cdot(MA)_1\cdot(HMHP)_1$ cluster, indicating the introduction of HMHP molecules strengthens the HB interactions within the system. Besides, in clusters involving HMHP (Fig. S2), HMHP facilitates the formation of cage-like clusters with MSA and MA through a spatial network of HBs. Notably, proton transfer is observed in ternary clusters involving HMHP. Taken together, these findings suggest that HMHP forms stable clusters with MSA and MA via both HBs and proton transfer, thereby enhancing the stability of the MSA-MA-HMHP clusters.

3.3.2 Cluster stability analysis

To evaluate the effect of HMHP on the thermodynamic stability of MSA-MA-clusters, the Gibbs free energy

(ΔG) (Table S7) and total evaporation rates ($\Sigma\gamma$) (Table S10) of clusters in the MSA-MA-HMHP system were calculated. The ΔG of HMHP-involved clusters are consistently lower than those of the corresponding pure MSA-MA clusters, indicating that the participation of HMHP enhances cluster thermodynamic stability. Consistent with the ΔG analysis, HMHP-containing clusters also exhibit markedly reduced $\Sigma\gamma$ values. In addition to thermodynamic stability, cluster growth tendencies play a crucial role in atmospheric cluster formation. From a kinetic perspective, cluster formation is governed by the competition between molecular collisions and evaporation processes. When the ratio of the collision frequency between a cluster and a monomer at concentration C to the total evaporation rate, expressed as $\beta C/\Sigma\gamma$, is higher than 1, the cluster is considered capable of sustained growth. Accordingly, as shown in Fig. 4, the $\beta C/\Sigma\gamma$ ratios were evaluated under various atmospheric conditions to assess the influence of HMHP on the growth behavior of MSA-MA clusters. Among the clusters examined, $(MSA)_2$, $(MSA)_2\cdot(MA)$, $(MSA)_2\cdot(MA)_2$, $(MSA)_3\cdot(MA)_2$, $(MSA)\cdot(MA)\cdot(HMHP)$ and $(MSA)_2\cdot(MA)_2\cdot(HMHP)$ display sufficient stability against evaporation, enabling further growth through collisions with additional monomers. Overall, these results suggest that HMHP is likely to participate in the nucleation process of MSA-MA clusters by enhancing their thermodynamic stability and increasing their potential for sustained cluster growth.

3.3.3 Cluster formation pathways

To track the detailed nucleation pathways of HMHP involved in the formation of MSA-MA clusters, ACDC simulation were conducted at four different temperatures (238.15 K, 258.15 K, 278.15 K and 298.15 K), with concentrations set as [MSA] = 1.0×10^6 molecules·cm^{-3}, [MA] =2.5×10^8 molecules·cm^{-3} and [HMHP] = 1.0×10^{11} molecules·cm^{-3}. The results are presented in Fig. 5(a). At 238.15 K, the primary growth of the MSA-MA-HMHP system can be divided into two distinct routes. One pathway involves MSA-MA clustering alone, while the other incorporates HMHP molecules in the cluster formation process. In the HMHP involving pathway, HMHP initially interacts with the heterodimer $(MSA)_2\cdot(MA)_2$, resulting in the formation of a $(MSA)_2\cdot(MA)_2\cdot(HMHP)$ trimer. This trimer then grows out of the simulated system. Following this, the $(MSA)_2\cdot(MA)_2\cdot(HMHP)$ trimer collides with an MSA monomer, forming the cluster $(MSA)_3\cdot(MA)_2\cdot(HMHP)$. Subsequently, HMHP evaporates from this cluster, leaving behind the $(MSA)_3\cdot(MA)_2$ cluster. Finally, the $(MSA)_3\cdot(MA)_2$ trimer interacts with an MA monomer, resulting in the $(MSA)_3\cdot(MA)_3$ cluster, which eventually exits the system. These processes illustrate HMHP's dual function: it acts both as a "catalyst" that promotes the formation of MSA-MA clusters and as a "participant" in the assembly of critical clusters. This dual role is also observed at 258.15 K. However, at 278.15 K, HMHP acts only as a "participant" in the formation of critical clusters. With increasing temperature, the contribution of HMHP to

cluster formation diminishes, and at 298.15 K (Fig. S3) cluster formation occurs exclusively through the pure binary MSA-MA pathway. The higher evaporation coefficient of clusters at elevated temperatures leads to their faster evaporation. Together, these findings underscore the significant and direct role of HMHP in MSA-MA nucleation, effectively facilitating cluster formation across different temperatures.

To further investigate the influence of temperature (T) on HMHP's participation role in the MSA-MA nucleation process, we analyzed the contribution of different clustering pathways to the outward flux under varying T. As shown in Fig. 5(b), with increasing T, the dominance of HMHP-involved pathways gradually diminishes. At 238.15-258.15 K, the HMHP-involved pathway accounts for 63%, whereas at 278.15 K, the contribution decreases to 21%. These results highlight the significant role of low temperatures in facilitating HMHP's participation in MSA-MA nucleation. In addition to T, the contribution of nucleating precursor flux also significantly affects trace substances' involvement in the MSA-MA nucleation process. The contribution of HMHP to the MSA-MA system was found to be relatively insensitive to [MA], as illustrated in Fig. S3. In contrast, it is strongly influenced by [MSA], as depicted in Fig. 5(c). As [MSA] increases from 10^4 to 10^8 molecules·cm^{-3}, the contribution of HMHP-involved pathways decreases from 65% to 40%. At the low [MSA] (10^4-10^6 molecules·cm^{-3}), HMHP involvement remains substantial, accounting for 65% of the pathway. Overall, this study reveals that HMHP's contribution to MSA-MA nucleation is most pronounced under conditions of low T, and low concentrations of both MSA and MA.

3.4 Atmospheric implications of HMHP to MSA-MA system

Building on the above findings, low T coupled with low [MSA] and [MA] appear to favor an enhanced role of HMHP in MSA-MA nucleation. To assess the atmospheric significance of these variations, we quantified the contributions of MSA-MA cluster growth pathways, with and without HMHP involvement (Fig. 6), under favorable conditions of temperature (T = 258.15 K) and precursor concentrations ([MSA] = 1.00×10^4 molecules·cm^{-3}, [MA] = 2.50×10^7 molecules·cm^{-3}). Indeed, substantial variability in atmospheric HMHP concentrations has been observed across diverse environments worldwide. For example, levels range from 2.50×10^9 to 6.25×10^9 molecules·cm^{-3} in Central Portugal, Pabstthum, and Beijing. Higher concentrations, between 1.15×10^{10} to 3.00×10^{10} molecules·cm^{-3}, have been observed in Guang Zhou and Niwot Ridge, while the Southeastern United States exhibit the highest concentrations, reaching up to 1.25×10^{11} molecules·cm^{-3}. As shown in Fig. 6, in low [HMHP] regions such as Pabstthum and Beijing, HMHP-involved pathways account for only 11% and 12% of total NPF, respectively. In contrast, in environments characterized by high HMHP concentrations, such as the southeastern United States (1.25×10^{11} molecules·cm^{-3}) and Niwot Ridge (3.00×10^{10} molecules·cm^{-3}), HMHP-involving

nucleation pathways become dominant. Under these conditions, HMHP acts both as a "catalyst", facilitating the formation of MSA-MA clusters, and as an "participant" in the assembly of critical clusters (Figs. S5 and S6). These two roles contribute up to 59% and 42%, respectively, to the overall nucleation process. These results highlight that HMHP exerts a markedly stronger influence on MSA-MA nucleation at elevated concentrations, particularly in urban industrial regions, where its contribution to NPF can be substantial.

Previous studies have revealed that SA-MA and SA-A nucleation mechanisms are widely regarded as key contributors to new particle formation in urban industrial regions (Yin et al., 2021; Liu et al., 2021). To underscore the importance of MSA-MA-HMHP nucleation in urban industrial regions, the cluster formation rates (J) of the MSA-MA-HMHP system have been compared with those of the SA-MA and SA-A systems (Qiao et al., 2024) (Fig. S7). The results show that, over the temperature range of 238.15 K-298.15 K, the J of MSA-MA-HMHP system is 1-5 orders of magnitude higher than that of SA-MA system at equivalent precursor concentrations ([SA] = 1.00×10^6 molecules·cm^{-3} and [MA] = 1.00×10^8 molecules·cm^{-3}). Similarly, under the conditions of [SA] = 1.00×10^6 molecules·cm^{-3} and [A] = 1.00×10^{10} molecules·cm^{-3}, the J of MSA-MA-HMHP systems slightly exceeds that of SA-A system by approximately 5-6 orders of magnitude. These comparisons suggest that HMHP plays a key role in enhancing MSA-MA nucleation, particularly in urban industrial environments.

4. Conclusions

The hydrolysis of CH_2OO by MSA, occurring in both the gas phase and at interfaces and resulting in hydroxymethyl hydroperoxide (HMHP) formation, was investigated. In addition, the role of HMHP in promoting MSA-MA nucleation was elucidated.

Quantum chemical calculations suggest that the activation energy for HMHP formation via MSA-catalyzed gaseous hydrolysis of CH_2OO is relatively low, observed to be 2.9 kcal mol^{-1}. At a concentration of [MSA] = 10^6-10^8 molecules·cm^{-3}, MSA exhibits a dominant catalytic effect compared to other catalysts, such as NH_3 ([NH_3] = 10^7-10^{11} molecules·cm^{-3}), within the temperature range of 280.0-320.0 K. Notably, the computed effective rate constant for MSA is larger by about 2-6 orders of magnitude compared with that of NH_3. Simultaneously, when [MSA] = 10^5-10^8 molecules·cm^{-3}, k'_{MSA} is found to be 1 to 3 orders of magnitude larger than k'_{SA}, which corresponds to [SA] = 10^4-10^7 molecules·cm^{-3}. BOMD simulations further demonstrate that the MSA-catalyzed CH_2OO hydrolysis at the gas-liquid interface follows a ring-based reaction mechanism on a picosecond timescale. Remarkably, HMHP formation through MSA-catalyzed CH_2OO hydrolysis occurs rapidly and stably at the interface.

HMHP participates in MSA-MA-driven ternary nucleation through its bifunctional hydrogen-bonding capacity,

which allows direct association with both MSA and MA. Thermodynamic analysis shows that MSA-MA-HMHP trimers possess lower Gibbs free energy than MSA-MA dimers, indicating enhanced cluster stability. Cluster formation pathways analysis reveals a temperature-dependent role: at 238.15 K and 258.15 K, HMHP functions as both catalyst and participant, whereas at 278.15 K it acts solely as a participant due to increased evaporation rates. Under low temperature, low [MSA] and [MA], and high [HMHP] conditions, particularly in Niwot Ridge and the southeastern United States, HMHP-involved pathways contribute up to 59% and 42% of total nucleation flux. These results predict that HMHP substantially enhances MSA-MA-driven NPF in urban industrial regions, helping to explain previously unaccounted NPF sources and improve nucleation models.

Overall, this work deepens the understanding of hydroperoxide formation in MSA-polluted regions, especially at the gas-liquid interface. It also reveals the potential contribution of other organic peroxides to NPF, offering a plausible explanation for part of the unaccounted particle fluxes in urban industrial regions.

Data availability

Data will be made available on request.

Authorship contributions

RL: methodology, investigation, data curation, writing (original draft). ZL: writing (review), data curation, methodology, investigation. CZ: writing (review), data computation. JY: data curation, data computation. HC: writing (editing), data curation, visualization, investigation. XL: writing (review and editing). NH: data curation, project administration, writing (review and editing). RW: funding acquisition, writing (review and editing). TZ: writing (review and editing), funding acquisition.

Competing interests

The authors declare that they have no known competing financial interests or personal relationships that could have appeared to influence the work reported in this paper.

Acknowledgements

This work was supported by the National Natural Science Foundation of China (No: 22203052; 22073059), the Funds of Graduate Innovation of Shaanxi University of Technology (No: SLGYCX2506).

References

Allen, H. M., Crounse, J. D., Bates, K. H., Teng, A. P., Krawiec-Thayer, M. P., Rivera-Rios, J. C., Keutsch, F. N., St. Clair, J. M., Hanisco, T. F., Møller, K. H., Kjaergaard, H. G., and Wennberg, P. O.: Kinetics and Product Yields of the OH

Initiated Oxidation of Hydroxymethyl Hydroperoxide, J. Phys. Chem. A, 122, 6292-6302, https://doi.org/10.1021/acs.jpca.8b04577, 2018.

Anglada, J. M., Hoffman, G. J., Slipchenko, L. V., M.Costa, M., Ruiz-López, M. F., and Francisco, J. S.: Atmospheric Significance of Water Clusters and Ozone-Water Complexes, J. Phys. Chem. A, 117, 10381-10396, https://doi.org/10.1021/jp407282c., 2013.

Anglada, J. M., and Solé, A.: Impact of the water dimer on the atmospheric reactivity of carbonyl oxides, Phys. Chem. Chem. Phys., 18, 17698-17712, https://doi.org/10.1039/C6CP02531E., 2016.

Arquero, K. D., Gerber, R. B., and Finlayson-Pitts, B. J.: The Role of Oxalic Acid in New Particle Formation from Methanesulfonic Acid, Methylamine, and Water, Environ. Sci. Technol., 51, 2124-2130, https://doi.org/10.1021/acs.est.6b05056., 2017.

Barnes, I., Hjorth, J., and Mihalopoulos, N.: Dimethyl Sulfide and Dimethyl Sulfoxide and Their Oxidation in the Atmosphere, Chem. Rev., 106, 940-975, https://doi.org/10.1021/cr020529+, 2006.

Becke, A. D.: Density-functional exchange-energy approximation with correct asymptotic behavior, Phys. Rev. A, 38, 3098-3100, https://doi.org/10.1103/PhysRevA.38.3098., 1988.

Berndt, T., Kaethner, R., Voigtländer, J., Stratmann, F., Pfeifle, M., Reichle, P., Sipilä, M., Kulmala, M., and Olzmann, M.: Kinetics of the unimolecular reaction of CH_2OO and the bimolecular reactions with the water monomer, acetaldehyde and acetone under atmospheric conditions, Phys. Chem. Chem. Phys., 17, 19862-19873, https://doi.org/10.1039/C5CP02224J., 2015.

Berresheim, H., Elste, T., Tremmel, H. G., Allen, A. G., Hansson, H.-C., Rosman, K., Dal Maso, M., Mäkelä, J. M., Kulmala, M., and O'Dowd, C. D.: Gas-aerosol relationships of H_2SO_4, MSA, and OH: Observations in the coastal marine boundary layer at Mace Head, Ireland, J. Geophys. Res., 107, 1-12 , https://doi.org/10.1029/2000JD000229, 2002.

Chao, W., Hsieh, J.-T., Chang, C.-H., and Lin, J. J.-M.: Direct kinetic measurement of the reaction of the simplest Criegee intermediate with water vapor, Science, 347, 751-754, https://doi.org/10.1126/science.1261549., 2015.

Chao, W., Yin, C., Takahashi, K., and Lin, J. J.-M.: Effects of water vapor on the reaction of CH_2OO with NH_3, Phys. Chem. Chem. Phys., 21, 22589-22597, https://doi.org/10.1039/C9CP04682H., 2019.

Chen, D., Li, D., Wang, C., Liu, F., and Wang, W.: Formation mechanism of methanesulfonic acid and ammonia clusters: A kinetics simulation study, Atmos. Environ., 222, 117161, https://doi.org/10.1016/j.atmosenv.2019.117161, 2020.

Chen, H., Varner, M. E., Gerber, R. B., and Finlayson-Pitts, B. J.: Reactions of Methanesulfonic Acid with Amines and Ammonia as a Source of New Particles in Air, J. Phys. Chem. B, 120, 1526-1536, https://doi.org/10.1021/acs.jpcb.5b07433., 2016.

Cheng, Y., Ding, C., Zhang, T., Wang, R., Mu, R., Li, Z., Li, R., Shi, J., and Zhu, C.: Barrierless reactions of C2 Criegee intermediates with H_2SO_4 and their implication to oligomers and new particle formation, J. Environ. Sci., 149, 574-584, https://doi.org/10.1016/j.jes.2023.12.020., 2025.

Ding, C., Wen, M., Zhang, T., Li, Z., Li, R., Wang, R., Ou, T., Song, F., and Zhang, Q.: Molecular mechanisms and atmospheric implications of the simplest criegee intermediate and hydrochloric acid chemistry in the gas phase and at the aqueous interfaces, Atmos. Environ., 330, 120558, https://doi.org/10.1016/j.atmosenv.2024.120558., 2024.

Dong, Z., Francisco, J. S., and Long, B.: Ammonolysis of Glyoxal at the Air-Water Nanodroplet Interface, Angew. Chem. Int. Ed., 63, e202316060, https://doi.org/10.1002/anie.202316060, 2024.

Elm, J.: Clusteromics II: Methanesulfonic Acid-Base Cluster Formation, ACS omega, 6, 17035-17044, https://doi.org/10.1021/acsomega.1c02115., 2021.

Fang, Y.-G., Wei, L., Francisco, J. S., Zhu, C., and Fang, W.-H.: Mechanistic Insights into Chloric Acid Production by Hydrolysis of Chlorine Trioxide at an Air-Water Interface, J. Am. Chem. Soc., 146, 21052-21060, https://doi.org/10.1021/jacs.4c06269., 2024.

Gaston, C. J., Pratt, K. A., Qin, X., and Prather, K. A.: Real-Time Detection and Mixing State of Methanesulfonate in Single Particles at an Inland Urban Location during a Phytoplankton Bloom, Environ. Sci. Technol., 44, 1566-1572, https://doi.org/10.1021/es902069d, 2010.

Glowacki, D. R., Liang, C.-H., Morley, C., Pilling, M. J., and Robertson, S. H.: MESMER: An Open-Source Master Equation Solver for Multi-Energy Well Reactions, J. Phys. Chem. A, 116, 9545-9560, https://doi.org/10.1021/jp3051033., 2012.

Goedecker, S., Teter, M., and Hutter, J.: Separable dual-space Gaussian pseudopotentials, Phys. Rev. B, 54, 1703-1710, https://doi.org/10.1103/PhysRevB.54.1703., 1996.

Grimme, S., Antony, J., Ehrlich, S., and Krieg, H.: A consistent and accurate ab initio parametrization of density functional dispersion correction (DFT-D) for the 94 elements H-Pu, J. Chem. Phys., 132, https://doi.org/10.1063/1.3382344., 2010.

Grossmann, D., Moortgat, G. K., Kibler, M., Schlomski, S., Bächmann, K., Alicke, B., Geyer, A., Platt, U., Hammer, M.-U., Vogel, B., Mihelcic, D., Hofzumahaus, A., Holland, F., and Volz-Thomas, A.: Hydrogen peroxide, organic peroxides, carbonyl compounds, and organic acids measured at Pabstthum during BERLIOZ, J. Geophys. Res. Atmos., 108, https://doi.org/10.1029/2001JD001096, 2003.

Hewitt, C. N., and Kok, G. L.: Formation and occurrence of organic hydroperoxides in the troposphere: Laboratory and field observations, J. Atmos. Chem., 12, 181-194, https://link.springer.com/article/10.1007/BF00115779., 1991.

Hodshire, A. L., Campuzano-Jost, P., Kodros, J. K., Croft, B., Nault, B. A., Schroder, J. C., Jimenez, J. L., and Pierce, J. R.: The potential role of methanesulfonic acid (MSA) in aerosol formation and growth and the associated radiative forcings, Atmos. Chem. Phys., 19, 3137-3160, https://doi.org/10.5194/acp-19-3137-2019., 2019.

Hu, Y., Chen, S., Ye, S., Wei, S., Chu, B., Wang, R., Li, H., and Zhang, T.: The role of trifluoroacetic acid in new particle formation from methanesulfonic acid-methylamine, Atmos. Environ., 311, 120001, https://doi.org/10.1016/j.atmosenv.2023.120001, 2023.

Hutter, J., Iannuzzi, M., Schiffmann, F., and VandeVondele, J.: cp2k: atomistic simulations of condensed matter systems, WIREs Comput. Mol. Sci., 4, 15-25, https://doi.org/10.1002/wcms.1159, 2014.

Jackson, A. V., and Hewitt, C. N.: Hydrogen peroxide and organic hydroperoxide concentrations in air in a eucalyptus forest in central Portugal, Atmos. Environ., 30, 819-830, https://doi.org/10.1016/1352-2310(95)00348-7, 1996.

Khan, M. A. H., Percival, C. J., Caravan, R. L., Taatjes, C. A., and Shallcross, D. E.: Criegee intermediates and their impacts on the troposphere, Environ. Sci.: Processes Impacts, 20, 437-453, https://doi.org/10.1039/C7EM00585G., 2018.

Kumar, A., Mallick, S., and Kumar, P.: Oxidation of $HOSO^{\cdot}$ by $Cl^{\cdot}$: a new source of SO_2 in the atmosphere?, Phys. Chem. Chem. Phys., 23, 18707-18711, https://doi.org/10.1039/D1CP01048D., 2021.

Lee, J. H., Leahy, D. F., Tang, I. N., and Newman, L.: Measurement and speciation of gas phase peroxides in the atmosphere, J. Geophys. Res. Atmos., 98, 2911-2915, https://doi.org/10.1029/92JD02514, 1993.

Lee, S.-H., Gordon, H., Yu, H., Lehtipalo, K., Haley, R., Li, Y., and Zhang, R.: New Particle Formation in the Atmosphere: From Molecular Clusters to Global Climate, J. Geophys. Res. Atmos., 124, 7098-7146, https://doi.org/10.1029/2018JD029356, 2019.

Li, J., Ning, A., Liu, L., and Zhang, X.: Atmospheric Bases-Enhanced Iodic Acid Nucleation: Altitude-Dependent Characteristics and Molecular Mechanisms, Environ. Sci. Technol., 58, 16962-16973, https://doi.org/10.1021/acs.est.4c06053., 2024a.

Li, J., Wu, N., Chu, B., Ning, A., and Zhang, X.: Molecular-level study on the role of methanesulfonic acid in iodine oxoacid nucleation, Atmos. Chem. Phys., 24, 3989-4000, https://doi.org/10.5194/acp-24-3989-2024., 2024b.

Li, L., Zhang, Q., Wei, Y., Wang, Q., and Wang, W.: Theoretical Study on the Gas Phase and Gas-Liquid Interface Reaction Mechanism of Criegee Intermediates with Glycolic Acid Sulfate, Int. J. Mol. Sci., 24, 3355, https://doi.org/10.3390/ijms24043355., 2023.

Li, M., Li, L., Liu, S., Zhang, Q., Wang, W., and Wang, Q.: Insights into the catalytic effect of atmospheric organic trace species on the hydration of Criegee intermediates, Sci. Total Environ., 949, 174877, https://doi.org/10.1016/j.scitotenv.2024.174877, 2024c.

Lin, L.-C., Chang, H.-T., Chang, C.-H., Chao, W., Smith, M. C., Chang, C.-H., Jr-Min Lin, J., and Takahashi, K.: Competition between H_2O and $(H_2O)_2$ reactions with CH_2OO/CH_3CHOO, Phys. Chem. Chem. Phys., 18, 4557-4568, https://doi.org/10.1039/C5CP06446E., 2016.

Liu, J., Liu, L., Rong, H., and Zhang, X.: The potential mechanism of atmospheric new particle formation involving amino acids with multiple functional groups, Phys. Chem. Chem. Phys., 23, 10184-10195, https://doi.org/10.1039/D0CP06472F, 2021.

Liu, Y., Xie, H.-B., Ma, F., Chen, J., and Elm, J.: Amine-Enhanced Methanesulfonic Acid-Driven Nucleation: Predictive Model and Cluster Formation Mechanism, Environ. Sci. Technol., 56, 7751-7760, https://doi.org/10.1021/acs.est.2c01639., 2022.

Long, B., Bao, J. L., and Truhlar, D. G.: Atmospheric Chemistry of Criegee Intermediates: Unimolecular Reactions and Reactions with Water, J. Am. Chem. Soc., 138, 14409-14422, https://doi.org/10.1021/jacs.6b08655., 2016.

Mardirossian, N., and Head-Gordon, M.: How Accurate Are the Minnesota Density Functionals for Noncovalent Interactions, Isomerization Energies, Thermochemistry, and Barrier Heights Involving Molecules Composed of Main-Group Elements?, J. Chem. Theory Comput., 12, 4303-4325, https://doi.org/10.1021/acs.jctc.6b00637., 2016.

McGrath, M. J., Olenius, T., Ortega, I. K., Loukonen, V., Paasonen, P., Kurtén, T., Kulmala, M., and Vehkamäki, H.: Atmospheric Cluster Dynamics Code: a flexible method for solution of the birth-death equations, Atmos. Chem. Phys., 12, 2345-2355, https://doi.org/10.5194/acp-12-2345-2012., 2012.

Meana-Pañeda, R., Zheng, J., Bao, J. L., Zhang, S., Lynch, B. J., Corchado, J. C., Chuang, Y.-Y., Fast, P. L., Hu, W.-P., Liu, Y.-P., Lynch, G. C., Nguyen, K. A., Jackels, C. F., Fernández-Ramos, A., Ellingson, B. A., Melissas, V. S., Villà, J., Rossi, I., Coitiño, E. L., Pu, J., Albu, T. V., Zhang, R. M., Xu, X., Ratkiewicz, A., Steckler, R., Garrett, B. C., Isaacson, A. D., and Truhlar, D. G.: Polyrate 2023: A computer program for the calculation of chemical reaction rates for polyatomics. New version announcement, Comput. Phys. Commun., 294, 108933, https://doi.org/10.1016/j.cpc.2023.108933, 2024.

Neese, F.: The ORCA program system, Mol. Sci., 2, 73-78, https://doi.org/10.1002/wcms.81, 2012.

Newland, M. J., Rickard, A. R., Vereecken, L., Muñoz, A., Ródenas, M., and Bloss, W. J.: Atmospheric isoprene ozonolysis: impacts of stabilised Criegee intermediate reactions with SO_2, H_2O and dimethyl sulfide, Atmos. Chem. Phys., 15, 9521-9536, https://doi.org/10.5194/acp-15-9521-2015., 2015.

Nguyen, T. B., Crounse, J. D., Teng, A. P., St. Clair, J. M., Paulot, F., Wolfe, G. M., and Wennberg, P. O.: Rapid deposition of oxidized biogenic compounds to a temperate forest, Proc. Natl. Acad. Sci. U.S.A., 112, E392-E401, https://doi.org/10.1073/pnas.1418702112., 2015.

Ning, A., Liu, L., Ji, L., and Zhang, X.: Molecular-level nucleation mechanism of iodic acid and methanesulfonic acid, Atmos. Chem. Phys., 22, 6103-6114, https://doi.org/10.5194/acp-22-6103-2022., 2022.

Ning, A., and Zhang, X.: The synergistic effects of methanesulfonic acid (MSA) and methanesulfinic acid (MSIA) on marine new particle formation, Atmos. Environ., 269, 118826, https://doi.org/10.1016/j.atmosenv.2021.118826, 2022.

Ning, A., Shen, J., Zhao, B., Wang, S., Cai, R., Jiang, J., Yan, C., Fu, X., Zhang, Y., Li, J., Ouyang, D., Sun, Y., Saiz-Lopez, A., Francisco, J. S., and Zhang, X.: Overlooked significance of iodic acid in new particle formation in

the continental atmosphere, Proc. Natl. Acad. Sci. U.S.A., 121, e2404595121, https://doi.org/10.1073/pnas.2404595121., 2024.

Ouyang, B., McLeod, M. W., Jones, R. L., and Bloss, W. J.: NO_3 radical production from the reaction between the Criegee intermediate CH_2OO and NO_2, Phys. Chem. Chem. Phys., 15, 17070-17075, https://doi.org/10.1039/C3CP53024H., 2013.

Partanen, L., Vehkamäki, H., Hansen, K., Elm, J., Henschel, H., Kurtén, T., Halonen, R., and Zapadinsky, E.: Effect of Conformers on Free Energies of Atmospheric Complexes, J. Phys. Chem. A, 120, 8613-8624, https://doi.org/10.1021/acs.jpca.6b04452., 2016.

Pereira, A. T., Ribeiro, A. J. M., Fernandes, P. A., and Ramos, M. J.: Benchmarking of density functionals for the kinetics and thermodynamics of the hydrolysis of glycosidic bonds catalyzed by glycosidases, Int. J. Quantum Chem., 117, e25409, https://doi.org/10.1002/qua.25409, 2017.

Perraud, V., Horne, J. R., Martinez, A. S., Kalinowski, J., Meinardi, S., Dawson, M. L., Wingen, L. M., Dabdub, D., Blake, D. R., Gerber, R. B., and Finlayson-Pitts, B. J.: The future of airborne sulfur-containing particles in the absence of fossil fuel sulfur dioxide emissions, Proc. Natl. Acad. Sci. U.S.A., 112, 13514-13519, https://doi.org/10.1073/pnas.1510743112., 2015.

Phillips, J. C., Braun, R., Wang, W., Gumbart, J., Tajkhorshid, E., Villa, E., Chipot, C., Skeel, R. D., Kalé, L., and Schulten, K.: Scalable molecular dynamics with NAMD, J. Comput Chem., 26, 1781-1802, https://doi.org/10.1002/jcc.20289, 2005.

Qiao, F., Zhang, R., Zhao, Q., Ma, F., Chen, J., and Xie, H.-B.: A Surprisingly High Enhancing Potential of Nitric Acid in Sulfuric Acid–Methylamine Nucleation, Atmosphere,15, 467, https://doi.org/10.3390/atmos15040467, 2024.

Rissanen, M. P., Kurtén, T., Sipilä, M., Thornton, J. A., Kangasluoma, J., Sarnela, N., Junninen, H., Jørgensen, S., Schallhart, S., Kajos, M. K., Taipale, R., Springer, M., Mentel, T. F., Ruuskanen, T., Petäjä, T., Worsnop, D. R., Kjaergaard, H. G., and Ehn, M.: The Formation of Highly Oxidized Multifunctional Products in the Ozonolysis of Cyclohexene, J. Am. Chem. Soc., 136, 15596-15606, https://doi.org/10.1021/ja507146s, 2014.

Sakamoto, Y., Inomata, S., and Hirokawa, J.: Oligomerization Reaction of the Criegee Intermediate Leads to Secondary Organic Aerosol Formation in Ethylene Ozonolysis, J. Phys. Chem. A, 117, 12912-12921, https://doi.org/10.1021/jp408672m., 2013.

Shen, J., Elm, J., Xie, H.-B., Chen, J., Niu, J., and Vehkamäki, H.: Structural Effects of Amines in Enhancing Methanesulfonic Acid-Driven New Particle Formation, Environ. Sci. Technol., 54, 13498-13508, https://doi.org/10.1021/acs.est.0c05358., 2020.

Stone, D., Blitz, M., Daubney, L., Howes, N. U. M., and Seakins, P.: Kinetics of CH_2OO reactions with SO_2, NO_2, NO, H_2O and CH_3CHO as a function of pressure, Phys. Chem. Chem. Phys, 16, 1139-1149, https://doi.org/10.1039/C3CP54391A., 2014.

Tang, B., Bai, Q., Fang, Y.-G., Francisco, J. S., Zhu, C., and Fang, W.-H.: Mechanistic Insights into N_2O_5-Halide Ions Chemistry at the Air-Water Interface, J. Am. Chem. Soc., 146, 21742-21751, https://doi.org/10.1021/jacs.4c05850., 2024.

Tröstl, J., Chuang, W. K., Gordon, H., Heinritzi, M., Yan, C., Molteni, U., Ahlm, L., Frege, C., Bianchi, F., Wagner, R., Simon, M., Lehtipalo, K., Williamson, C., Craven, J. S., Duplissy, J., Adamov, A., Almeida, J., Bernhammer, A.-K., Breitenlechner, M., Brilke, S., Dias, A., Ehrhart, S., Flagan, R. C., Franchin, A., Fuchs, C., Guida, R., Gysel, M., Hansel, A., Hoyle, C. R., Jokinen, T., Junninen, H., Kangasluoma, J., Keskinen, H., Kim, J., Krapf, M., Kürten, A., Laaksonen, A., Lawler, M., Leiminger, M., Mathot, S., Möhler, O., Nieminen, T., Onnela, A., Petäjä, T., Piel, F. M., Miettinen, P., Rissanen, M. P., Rondo, L., Sarnela, N., Schobesberger, S., Sengupta, K., Sipilä, M., Smith, J. N., Steiner, G., Tomè, A., Virtanen, A., Wagner, A. C., Weingartner, E., Wimmer, D., Winkler, P. M., Ye, P., Carslaw, K. S., Curtius, J., Dommen, J., Kirkby, J., Kulmala, M., Riipinen, I., Worsnop, D. R., Donahue, N. M., and Baltensperger,

U.: The role of low-volatility organic compounds in initial particle growth in the atmosphere, Nature, 533, 527-531, https://doi.org/10.1038/nature18271., 2016.

Tsona Tchinda, N., Du, L., Liu, L., and Zhang, X.: Pyruvic acid, an efficient catalyst in SO_3 hydrolysis and effective clustering agent in sulfuric-acid-based new particle formation, Atmos. Chem. Phys., 22, 1951-1963, https://doi.org/10.5194/acp-22-1951-2022., 2022.

Wang, H., Wei, S., Yang, J., Yang, Y., Li, R., Wang, R., Zhu, C., Zhang, T., and Zhang, C.: A novel formation mechanism of sulfamic acid and its enhancing effect on methanesulfonic acid–methylamine aerosol particle formation in agriculture-developed and coastal industrial areas, Atmos. Chem. Phys., 25, 2829-2844, https://doi.org/10.5194/acp-25-2829-2025., 2025.

Wang, R., Wen, M., Chen, X., Mu, R., Zeng, Z., Chai, G., Lily, M., Wang, Z., and Zhang, T.: Atmospheric Chemistry of CH_2OO: The Hydrolysis of CH_2OO in Small Clusters of Sulfuric Acid, J. Phys. Chem. A, 125, 2642-2652, https://doi.org/10.1021/acs.jpca.1c02006., 2021a.

Wang, R., Wen, M., Liu, S., Lu, Y., Makroni, L., Muthiah, B., Zhang, T., Wang, Z., and Wang, Z.: The favorable routes for the hydrolysis of CH_2OO with H_2O_n (n = 1-4) investigated by global minimum searching combined with quantum chemical methods, Phys. Chem. Chem. Phys., 23, 12749-12760, https://doi.org/10.1039/D0CP00028K., 2021b.

Wang, S., Zhao, Y., Chan, A. W. H., Yao, M., Chen, Z., and Abbatt, J. P. D.: Organic Peroxides in Aerosol: Key Reactive Intermediates for Multiphase Processes in the Atmosphere, Chem. Rev., 123, 1635-1679, https://doi.org/10.1021/acs.chemrev.2c00430., 2023.

Wei, S., Wan, Q., Zhou, S., Nie, W., and Chen, S.: Spontaneous Generation of $^{-}CH_2CN$ from Acetonitrile at the Air-Water Interface, J. Am. Chem. Soc., 146, 32777-32784, http://doi.org/10.1021/jacs.4c13013, 2024.

Wen, H., Huang, T., Wang, C.-Y., Peng, X.-Q., Jiang, S., Liu, Y.-R., and Huang, W.: A study on the microscopic mechanism of methanesulfonic acid-promoted binary nucleation of sulfuric acid and water, Atmos. Environ., 191, 214-226, https://doi.org/10.1016/j.atmosenv.2018.07.050, 2018.

Wu, H., Fu, Y., Dong, W., Fu, B., and Zhang, D. H.: Full-dimensional neural network potential energy surface and dynamics of the $CH_2OO + H_2O$ reaction, RSC Adv., 13, 13397-13404, https://doi.org/10.1039/D3RA02069J., 2023a.

Wu, H., Fu, Y., Fu, B., and Zhang, D. H.: Roaming Dynamics in Hydroxymethyl Hydroperoxide Decomposition Revealed by the Full-Dimensional Potential Energy Surface of the $CH_2OO + H_2O$ Reaction, J. Phys. Chem. A, 127, 9098-9105, https://doi.org/10.1021/acs.jpca.3c05818., 2023b.

Wu, N., Ning, A., Liu, L., Zu, H., Liang, D., and Zhang, X.: Methanesulfonic acid and iodous acid nucleation: a novel mechanism for marine aerosols, Phys. Chem. Chem. Phys., 25, 16745-16752, https://doi.org/10.1039/d3cp01198d., 2023c.

Xu, J., Finlayson-Pitts, B. J., and Gerber, R. B.: Nanoparticles grown from methanesulfonic acid and methylamine: microscopic structures and formation mechanism, Phys. Chem. Chem. Phys., 19, 31949-31957, https://doi.org/10.1039/d3cp01198d., 2017a.

Xu, J., Finlayson-Pitts, B. J., and Gerber, R. B.: Proton Transfer in Mixed Clusters of Methanesulfonic Acid, Methylamine, and Oxalic Acid: Implications for Atmospheric Particle Formation, J. Phys. Chem. A, 121, 2377-2385, https://doi.org/10.1021/acs.jpca.7b01223, 2017b.

Xu, Q., Ma, F., Xia, D., Li, X., Chen, J., Xie, H.-B., and Francisco, J. S.: Two-Step Noncatalyzed Hydrolysis Mechanism of Imines at the Air-Water Interface, J. Am. Chem. Soc., 146, 28866-28873, https://doi.org/10.1021/jacs.4c09080., 2024.

Yan, J., Jung, J., Zhang, M., Xu, S., Lin, Q., Zhao, S., and Chen, L.: Significant Underestimation of Gaseous Methanesulfonic Acid (MSA) over Southern Ocean, Environ. Sci. Technol., 53, 13064-13070, https://doi.org/10.1021/acs.est.9b05362., 2019.

Yi, M. J. R. o. E. S.: The Study on Pollution of Atmospheric Photochemical Oxidants in Beijing, Res. Environ. Sci. 13, 14-17., https://en.cnki.com.cn/Article_en/CJFDTOTAL-HJXX200001003.htm., 2000.

Yin, R., Yan, C., Cai, R., Li, X., Shen, J., Lu, Y., Schobesberger, S., Fu, Y., Deng, C., Wang, L., Liu, Y., Zheng, J., Xie, H., Bianchi, F., Worsnop, D. R., Kulmala, M., and Jiang, J.: Acid-Base Clusters during Atmospheric New Particle Formation in Urban Beijing, Environ. Sci. Technol., 55, 10994-11005, https://doi.org/10.1021/acs.est.1c027011, 2021.

Zhang, J., and Dolg, M.: ABCluster: the artificial bee colony algorithm for cluster global optimization, Phys. Chem. Chem. Phys., 17, 24173-24181, https://doi.org/10.1039/C5CP04060D., 2015.

Zhang, R., Shen, J., Xie, H. B., Chen, J., and Elm, J.: The role of organic acids in new particle formation from methanesulfonic acid and methylamine, Atmos. Chem. Phys., 22, 2639-2650, https://doi.org/10.5194/acp-22-2639-2022., 2022.

Zhang, T., Lan, X., Wang, R., Roy, S., Qiao, Z., Lu, Y., and Wang, Z.: The catalytic effects of H_2CO_3, CH_3COOH, HCOOH and H_2O on the addition reaction of $CH_2OO + H_2O \rightarrow CH_2(OH)OOH$, Mol. Phys., 116, 1783-1794, https://doi.org/10.1080/00268976.2018.1454612., 2018.

Zhang, Y., ma, Y., Zeng, L., Shao, K., and Qi, B.: Study of atmospheric peroxides in Guangzhou city, China Environ. Sci., 21, 221-225, https://en.cnki.com.cn/Article_en/CJFDTOTAL-ZGHJ200103008.htm., 2001.

Zhang, Z., Yin, H., Shang, Y., and Luo, S.-N.: Accurate rate constants for barrierless dissociation of ethanol: VRC-VTST and SS-QRRK calculations with the cheaper DFT method, Chem. Phys. Lett., 823, 140522, https://doi.org/10.1016/j.cplett.2023.140522, 2023.

Zhang, Z. P., Wang, S. H., Shang, Y. L., Liu, J. H., and Luo, S. N.: Theoretical Study on Ethylamine Dissociation Reactions Using VRC-VTST and SS-QRRK Methods, J. Phys. Chem. A, 128, 2191-2199, https://doi.org/10.1021/acs.jpca.3c08373., 2024.

Zhao, H., Jiang, X., and Du, L.: Contribution of methane sulfonic acid to new particle formation in the atmosphere, Chemosphere, 174, 689-699, https://doi.org/10.1016/j.chemosphere.2017.02.040., 2017.

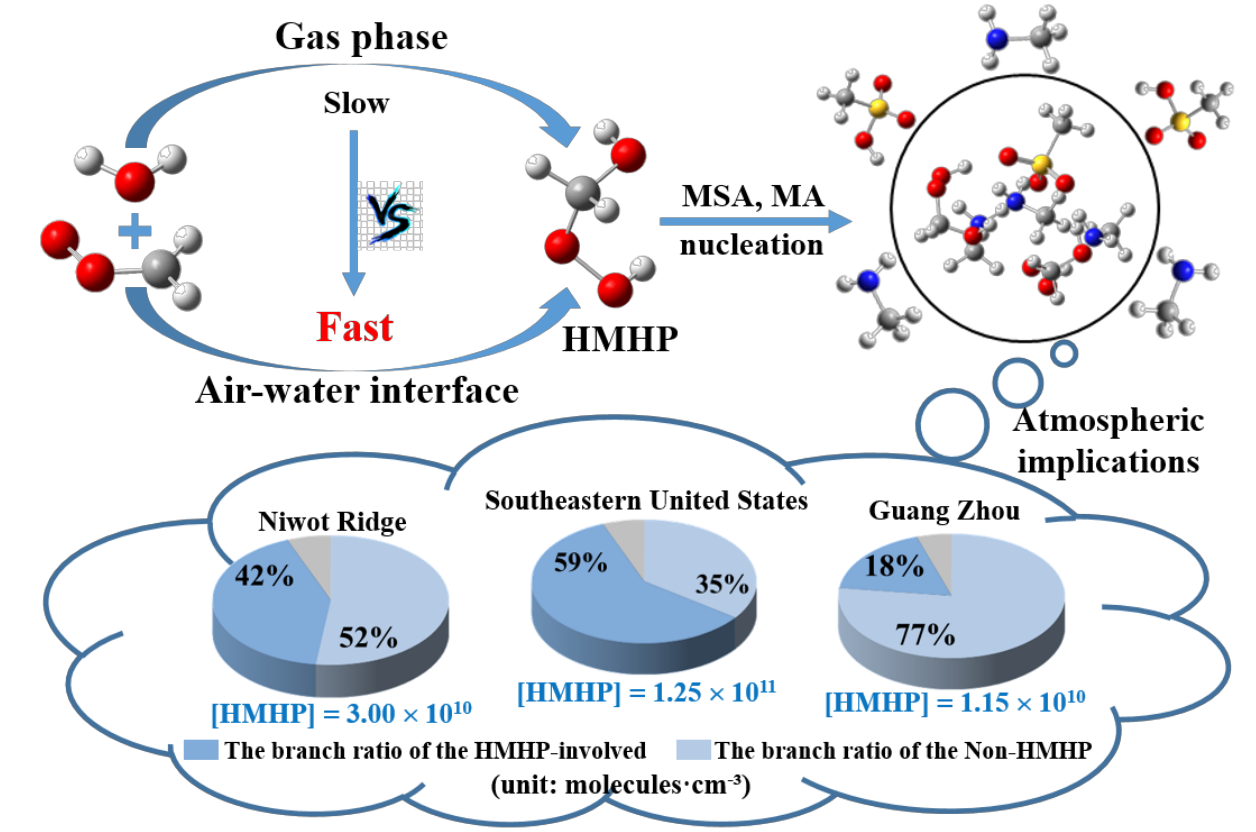

Graphic Abstract

Figure Captions

Fig. 1 Potential energy surface for the hydrolysis of CH_2OO without (a) and with H_2O (b) and CH_3SO_3H (c) at the CCSD(T)-F12/cc-pVDZ-F12//M06-2X/6-311++G(2*df*,2*pd*) level

Fig. 2 BOMD simulation trajectories and snapshots for CH_3SO_3H-mediated CH_2OO hydration at the water microdroplet interface

Fig. 3 (a) Electrostatic potential (ESP)-mapped molecular van der Waals (vdW) surface of MA, HMHP, and MSA calculated at M06-2X/6-311++G(2*df*, 2*pd*) + aug-cc-pVTZ level of theory. The orange and blue dots indicate the positions of ESP maximums and minimums (in kcal·mol^{-1}), with the corresponding values labeled in red and blue numbers, respectively. (b) The reduced density gradient (RDG) color-filled maps and isosurface of $(MSA)_1 \cdot (MA)_1$, $(MSA)_1 \cdot (MA)_1 \cdot (HMHP)_1$, and $(MSA)_1 \cdot (MA)_1 \cdot (HMHP)_2$ clusters.

Fig. 4 The $\log(\beta C/\Sigma\gamma)$ of $(MSA)_x(MA)_y(HMHP)_z$ ($0 \leqslant y \leqslant x + z \leqslant 3$) clusters at 238.15K. (a) without HMHP monomer, (b) containing a HMHP monomer. The $\beta C/\Sigma\gamma$ is the ratio of collision frequency between the cluster and monomer molecule at the concentration C to the total evaporation frequency at C = 2.5×10^8 molecules·cm^{-3}.

Fig. 5 Nucleation mechanism of the HMHP-MSA-MA system. (a) Cluster formation pathway at different temperatures; (b) the branch ratio of outward flux under varying [MSA] (1.0×10^4 -1.0×10^8 molecules·cm^{-3}); and (c) enhancement of the cluster formation rate (J, cm^{-3} s^{-1}).

Fig. 6 The branch ratio of the MSA-MA-HMHP (blue pie) and MSA-MA (light blue pie) growth pathways based on field data in different regions with a different [HMHP]. The data recorded in blue are from field observations, and those in black are set to be a median in this study. [MA] = 2.5×10^8 molecules·cm^{-3}. The map is from ©Google Maps (https://www.google.com/maps, last access: 15 July 2025)

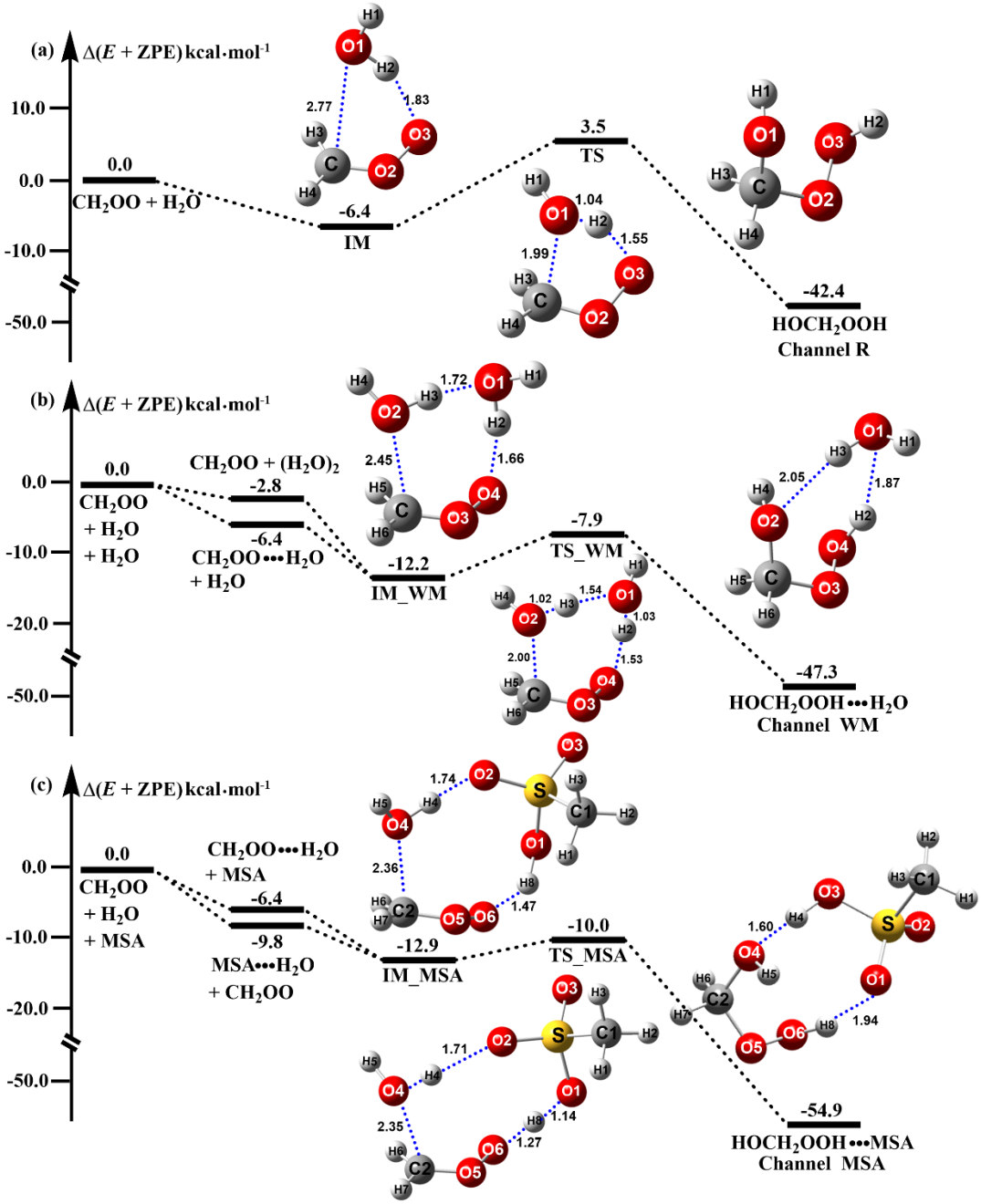

Fig. 1 Potential energy surface for the hydrolysis of CH_2OO without (a) and with H_2O (b) and CH_3SO_3H (c) at the CCSD(T)-F12/cc-pVDZ-F12//M06-2X/6-311++G(2*df*,2*pd*) level

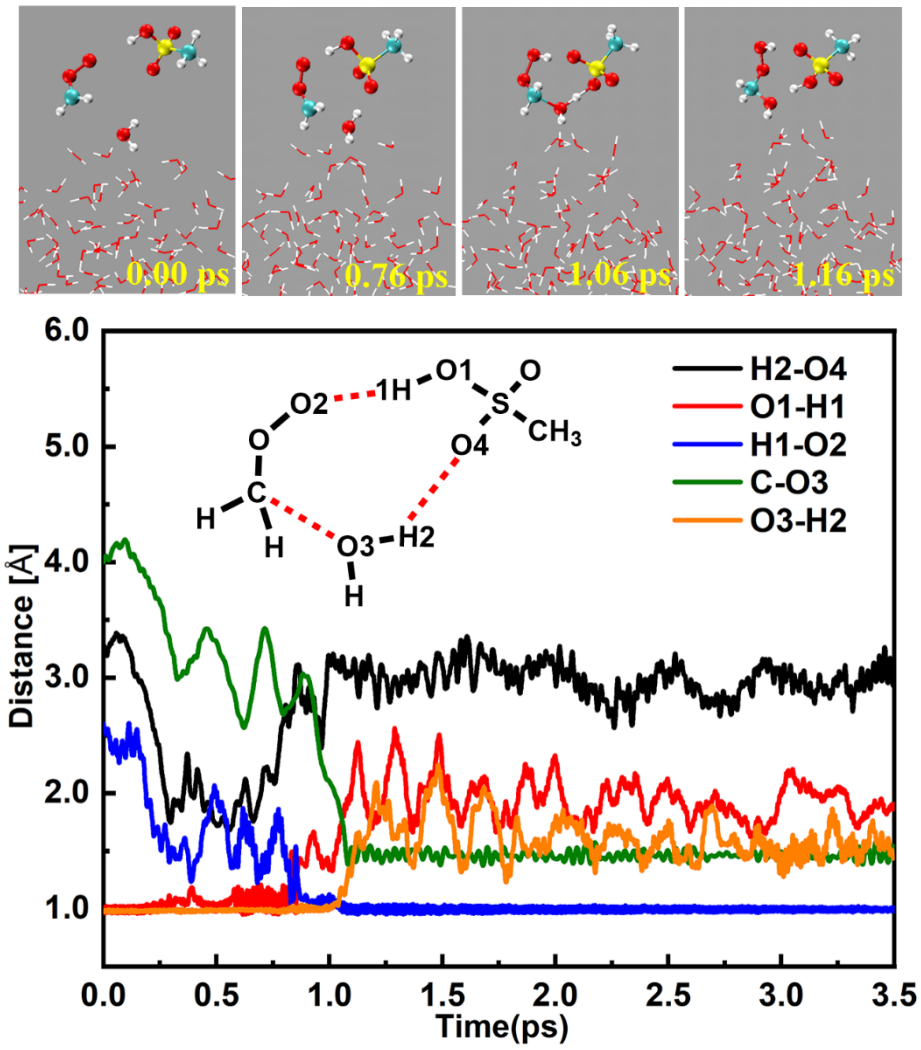

Fig. 2 BOMD simulation trajectories and snapshots for CH_3SO_3H-mediated CH_2OO hydration at the water microdroplet interface

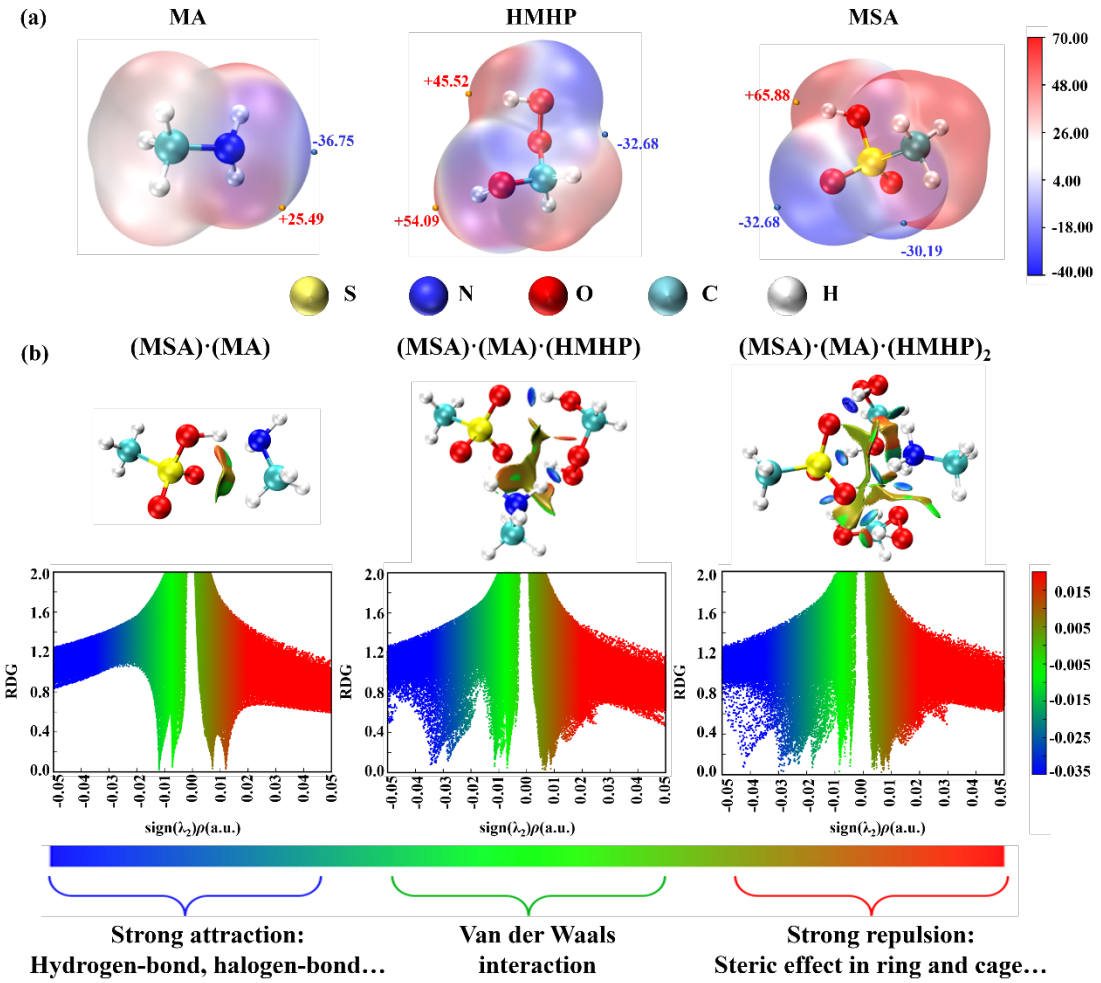

Fig. 3 (a) Electrostatic potential (ESP)-mapped molecular van der Waals (vdW) surface of MA, HMHP, and MSA calculated at M06-2X/6-311++G(2*df*, 2*pd*) + aug-cc-pVTZ level of theory. The orange and blue dots indicate the positions of ESP maximums and minimums (in kcal·mol^{-1}), with the corresponding values labeled in red and blue numbers, respectively. (b) The reduced density gradient (RDG) color-filled maps and isosurface of $(MSA)_1\cdot(MA)_1$, $(MSA)_1\cdot(MA)_1\cdot(HMHP)_1$, and $(MSA)_1\cdot(MA)_1\cdot(HMHP)_2$ clusters.

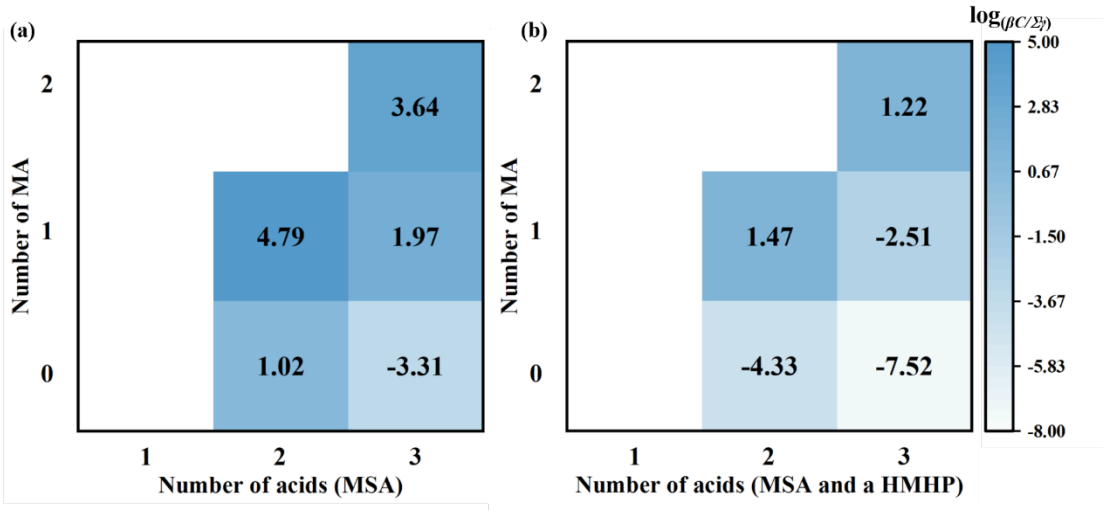

Fig. 4 The log(βC/$\Sigma\gamma$) of $(MSA)_x(MA)_y(HMHP)_z$ ($0 \leqslant y \leqslant x + z \leqslant 3$) clusters at 238.15K. (a) without HMHP monomer, (b) containing a HMHP monomer. The βC/$\Sigma\gamma$ is the ratio of collision frequency between the cluster and monomer molecule at the concentration C to the total evaporation frequency at $C = 2.5 \times 10^8$ molecules·cm^{-3}.

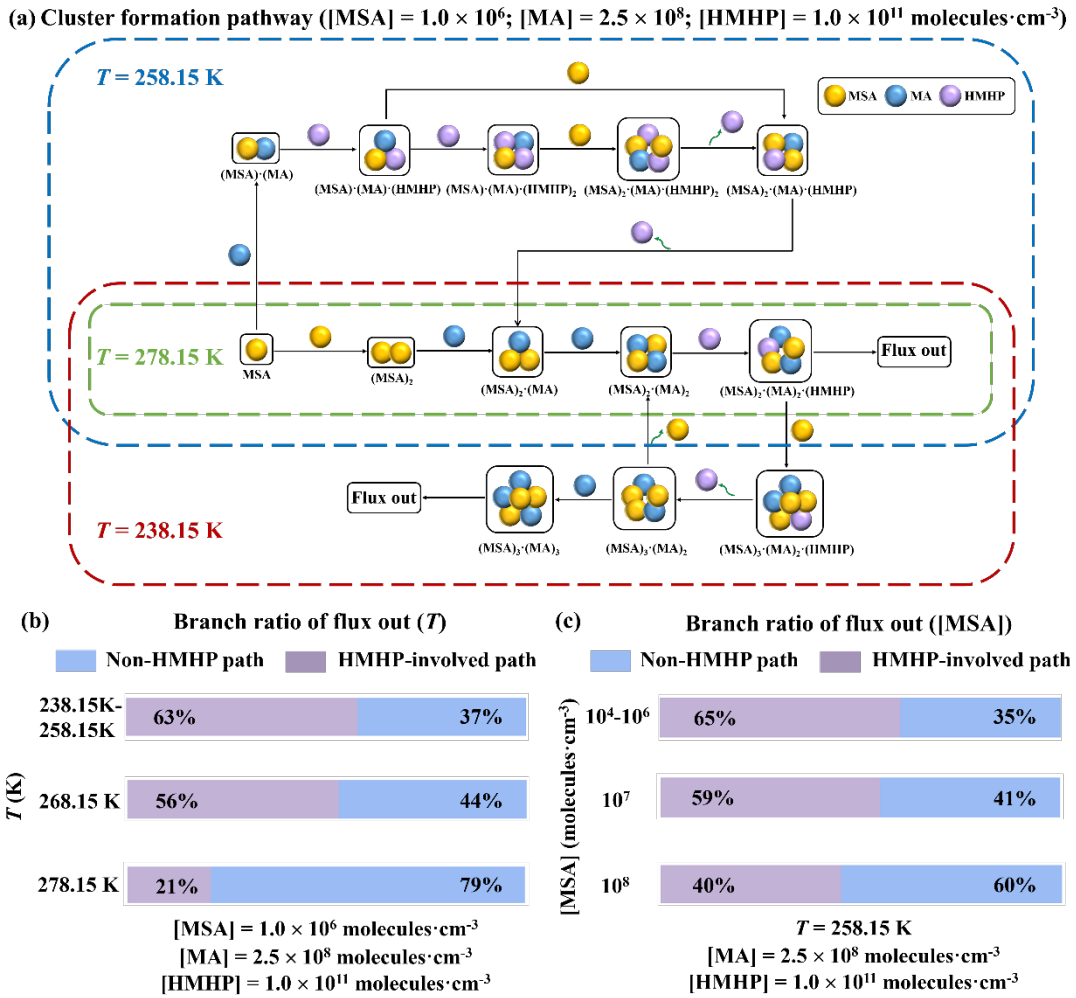

Fig. 5 Nucleation mechanism of the HMHP-MSA-MA system. (a) Cluster formation pathway at different temperatures; (b) the branch ratio of outward flux under varying [MSA] (1.0×10^4 -1.0×10^8 molecules·cm^{-3}); and (c) enhancement of the cluster formation rate (J, cm^{-3} s^{-1}).

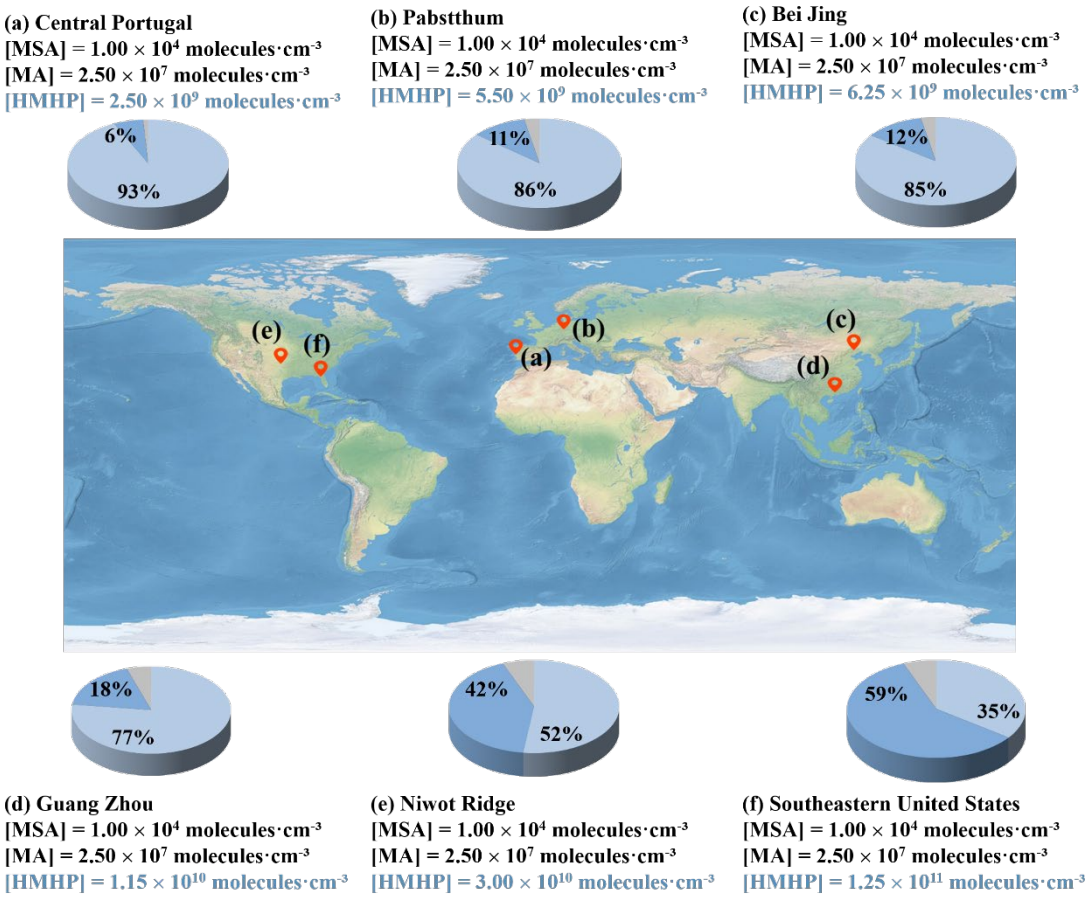

Fig.6 The branch ratio of the MSA-MA-HMHP (blue pie) and MSA-MA (light blue pie) growth pathways based on field data in different regions with a different [HMHP]. The data recorded in blue are from field observations, and those in black are set to be a median in this study. [MA] = 2.5 × 10^8 molecules·cm^{-3}. The map is from ©Google Maps (https://www.google.com/maps, last access: 15 July 2025)

Table 1 The rate ratio (r_1) between the interfacial MSA-catalyzed CH_2OO hydrolysis reaction and the corresponding reaction in the gas phase as well as the rate ratio (r_2) between the MSA-catalyzed CH_2OO hydrolysis reaction at the air-water nanodroplet interface and the hydrolysis of CH_2OO facilitated by H_2O in the gas phase at 298.0 K.

Rate ratio	r_1	r_2
	1.01×10^2	13.4